International Journal of Mechanical Sciences 300 (2025) 110484

Contents lists available at ScienceDirect

International Journal of Mechanical Sciences

journal homepage: www.elsevier.com/locate/ijmecsci

Enhancing load-bearing in lattice structures via core-modified designs with secondary hardening

Liming Huang [a], Jiafei Pang [a], Quanfeng Han [b], Jianxiang Wang [a,c,*], Xin Yi [a,c,*]

[a] School of Mechanics and Engineering Science, Peking University, Beijing 100871, China
[b] School of Automotive Engineering, Wuhan University of Technology, Wuhan 430070, China
[c] HEDPS, Center for Applied Physics and Technology, Peking University, Beijing 100871, China

ARTICLE INFO

Keywords:
Lattice structures
Additive manufacturing
Finite element analysis
Core reinforcement
Plastic deformation
Geometrical tuning

ABSTRACT

The mechanical performance of singly oriented lattice structures is often compromised by strength degradation caused by the evolution of local deformation bands. To address this challenge, a novel structural design strategy is proposed that utilizes a secondary hardening response to suppress the propagation of local shear bands in lattice structures. Fabricated via selective laser melting with 316L stainless steel, these structures are evaluated combining experimental and finite element analysis. Results reveal that core-modified lattice structures exhibit remarkable secondary hardening under large compressive deformation, delaying the propagation of local deformation bands through multi-step deformation and self-strengthening of the modified cores. Unit cell simulations confirm that the novel design enhances elastic modulus while reducing elastic anisotropy. Geometric parameter analysis demonstrates that plastic plateau and secondary hardening stages can be tailored by adjusting geometric features. The deformation mechanism analysis further attributes the secondary hardening response to the spatial distribution of plastic hinges, providing insights for advanced structural design.

1. Introduction

Architected materials with periodically arranged geometries, commonly referred to as lattice structures or structural metamaterials, have flourished with the advancements in additive manufacturing technologies due to their design flexibility, precise fabrication, and ability to achieve complex geometries unattainable by conventional methods [1]. These structures are utilized across industries such as automotive, biomedical, and aerospace for their unique combination of lightweight construction, high-performance mechanical properties, and customizable designs that can meet specific application demands [2–5]. Beyond their high strength-to-weight ratios, lattice structures exhibit novel mechanical behaviors, including negative thermal expansion [6], negative Poisson ratio [7,8], compression-torsion coupling [9], and electromechanical coupling effects [10].

Lattice structures can be categorized into stretching-dominated and bending-dominated types, as determined by Maxwell's topological criteria [11,12]. Stretching-dominated lattices, known for their higher Young's modulus and strength, are well suited for lightweight structural applications, whereas bending-dominated lattices offer greater compliance and energy absorption, making them ideal for impact mitigation [13,14]. Despite extensive efforts to optimize lattice configurations for improved Young's modulus, strength, and energy absorption [15–17], structural collapse under large deformation remains a key limitation, reducing load-bearing potential. During uniaxial compression, inhomogeneous plastic deformation leads to failure along specific planes, similar to dislocation slip in single crystals [18–20]. For lattices with singly oriented unit cells, the formation and propagation of shear bands during uniaxial loading pose a significant challenge, often leading to an extended plastic plateau with limited hardening capacity (Fig. 1a). Strategies to suppress shear band propagation are thus crucial for delaying plastic failure in lattice structures. Introducing a secondary hardening stage within the plastic plateau presents a promising approach to enhance the overall plastic response of the structure (Fig. 1b). The design strategies for unit cells and their impact on shear band evolution and structural performance are therefore explored in this study.

Inspired by polycrystalline microstructures, multi-phase lattices incorporating multi-phase hardening mechanisms have been developed to delay structural collapse by incorporating various unit cell types [20–25]. For example, dual-phase lattices with optimized reinforcement phase patterns and connectivity improve both strength and energy

* Corresponding authors.
E-mail addresses: jxwang@pku.edu.cn (J. Wang), xyi@pku.edu.cn (X. Yi).

https://doi.org/10.1016/j.ijmecsci.2025.110484
Received 12 January 2025; Received in revised form 5 June 2025; Accepted 7 June 2025
Available online 8 June 2025

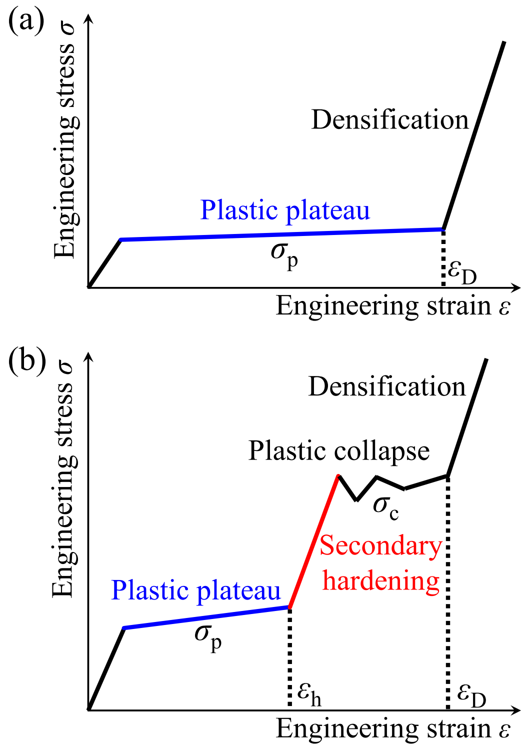

Fig. 1. Compressive engineering stress-strain (σ-ε) curves for lattice structures. (a) A prolonged plastic plateau accompanied by the evolution of localized shear deformation bands. (b) An enhanced plastic response characterized by the emergence of a secondary hardening stage. σ_p denotes the average plateau stress, ε_h represents the engineering strain at the onset of secondary hardening, σ_c denotes the plastic collapse stress after secondary hardening, and ε_D represents the engineering strain when reaching densification stage.

dissipation [21–24]. Multi-layer lattices with hybrid arrangements of distinct unit cell types further enhance ultimate strength and overall mechanical performance [25]. While multi-phase lattices effectively enhance structural properties, achieving a target mechanical response remains complex, requiring extensive tuning of phase arrangements through experiments and simulations. In contrast, designing and optimizing single-unit cells offers greater convenience and adaptability.

Following this direction, biomimetic hierarchical approaches have emerged as a powerful paradigm for developing high-performance lattice unit cells [26–29]. Hierarchical honeycombs with triangular lattice cell walls [26], strut-reinforced hierarchical designs [27], truss-plate-hybrids [28], and multi-feature bionic designs [29] demonstrate superior mechanical performances such as high modulus, progressive failure, and high energy absorption efficiency.

Beyond hierarchical architectures, component modifications introducing multi-plateau deformation characteristics have been explored for enhanced energy absorption. For example, designs featuring dual stress plateaus—such as double-arrowhead honeycombs [30], hybrid star honeycombs [31], reinforced octagonal honeycombs [32], reinforced I-beam-based lattices [33], topologically close-packed lattices [34], combinations of truss-tetrahedron and tetrakaidecahedron configurations [35], bio-inspired tube-plate structures [36], and nested-core configurations [37]—achieve superior energy dissipation and structural resilience. These multi-step deformation mechanisms closely resemble the secondary hardening behavior illustrated in Fig. 1b, validating the effectiveness of such design principles. The evident advantages of multi-step deformation warrant further investigations to expand the design framework, improve deformation resistance, and enable diverse multi-purpose applications.

This work presents a flexible and effective design strategy for lattice structures that enables tunable unit cell configurations and activates secondary hardening deformation behavior. We fabricate novel lattice structures incorporating core-modified (CM) unit cells using selective laser melting (SLM) technique and conduct compressive experiments to investigate their deformation behaviors and secondary hardening phenomena. Finite element modeling is employed to validate deformation mechanisms and mechanical performance, followed by parametric studies to analyze geometric effects on secondary hardening behavior. This CM design strategy offers a versatile framework for enhancing energy absorption efficiency and optimizing mechanical properties, paving the way for advanced lattice-based structural applications.

This paper is organized as follows. Section 2 outlines the design, fabrication, and testing methods for the CM lattice structures, along with the metrics for performance evaluation. Section 3 presents compression test results for both CM and conventional BCC lattices, supported by deformation analysis and simulation validation. Section 4 develops finite element models to investigate structural responses under both finite and small compressive strains. Section 5 explores the parametric dependence of mechanical behavior in the octet-based CM lattice, revealing deformation mechanisms and potential design strategies. Section 6 summarizes the key findings of this study.

2. Design and methods

This section outlines the structural design, fabrication, testing, and evaluation framework for the CM lattices. Section 2.1 introduces the design strategy and cell geometry; Section 2.2 describes the fabrication and mechanical testing procedures; and Section 2.3 defines the compressive performance metrics.

2.1. Structural design

In crystallography, variations in atomic arrangements and lattice constants give rise to different crystal lattices, forming a wide range of crystalline materials. Inspired by these, macroscopic lattice structures such as simple cubic (SC), body-centered cubic (BCC), all-face-centered cubic (AFCC), and octet lattices have been developed [38,39]. This study adopts the BCC lattice as the foundation for the CM design due to its stable, long stress plateau and bending-dominated behavior [13].

The CM design modifies the core region of the primary BCC lattice by altering the quantity and spatial distribution of its struts while preserving the exterior BCC framework. As shown in Fig. 2, three distinct lattice cells—SC-BCC, AFCC, and octet—are integrated into the core region (red), replacing the original struts to form CM-reinforced lattice cells (Fig. 2b). The exterior retains the BCC framework, while the core comprises the newly embedded lattice configuration, ensuring connectivity at the eight corner points of the core region. This approach allows the core region to accommodate diverse lattice configurations, offering enhanced design flexibility and structural adaptability. For simplicity, the CM unit cells are named according to their embedded core lattice types (e.g., SC-BCC, AFCC, and octet lattices in Fig. 2b). All proposed unit cells maintain cubic symmetry, and their principal directions are aligned with the edges of the cubic cell, oriented along the three orthogonal coordinate axes shown in Fig. 2a.

Fig. 3 illustrates the geometry of a CM unit cell with an SC-BCC core. The intersection point P marks the boundary between the core and exterior cells, where new strut branches extend into the core, deviating from the primary BCC lattice structure. The strut diameters of the core and exterior regions are denoted as d_1 and d_2, and L_1 and L_2 represent the core and overall unit cell sizes, respectively. Two dimensionless parameters are introduced

$$\alpha = d_2/d_1 - 1 \quad \text{and} \quad \beta = 2L_1/L_2 - 1,$$

where β ranges from -1 to 1, with $\beta = -1$ corresponding to the unmodified BCC lattice and $\beta = 1$ indicating a core cell that occupies the entire unit cell. Additionally, the strut angle θ is defined as the angle

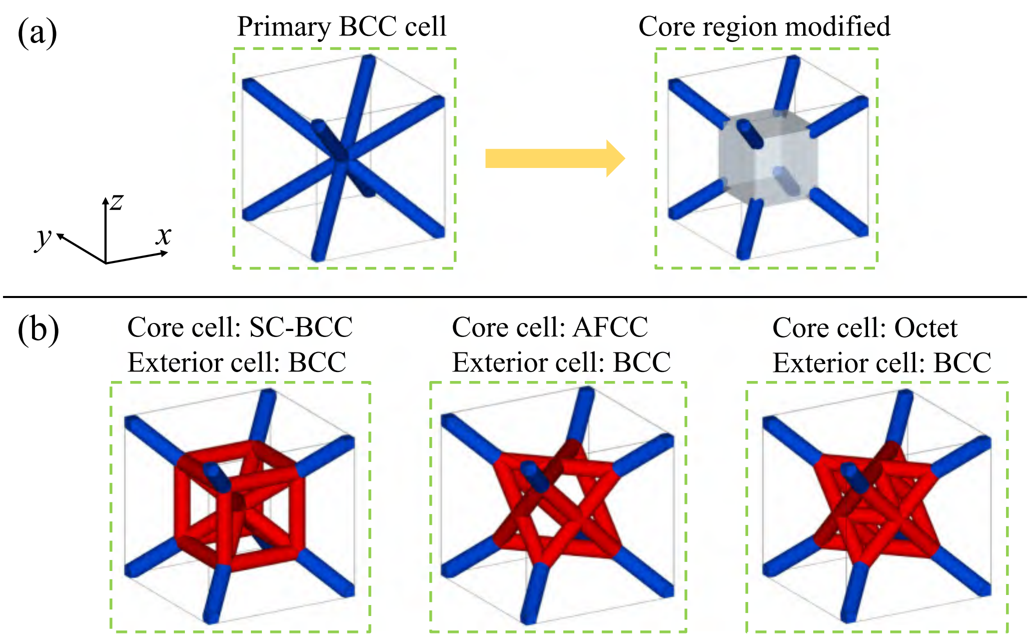

Fig. 2. Schematic illustration of the CM lattice designs. (a) Structural design strategy for CM lattices. (b) Geometrical configurations of lattices with core regions (red).

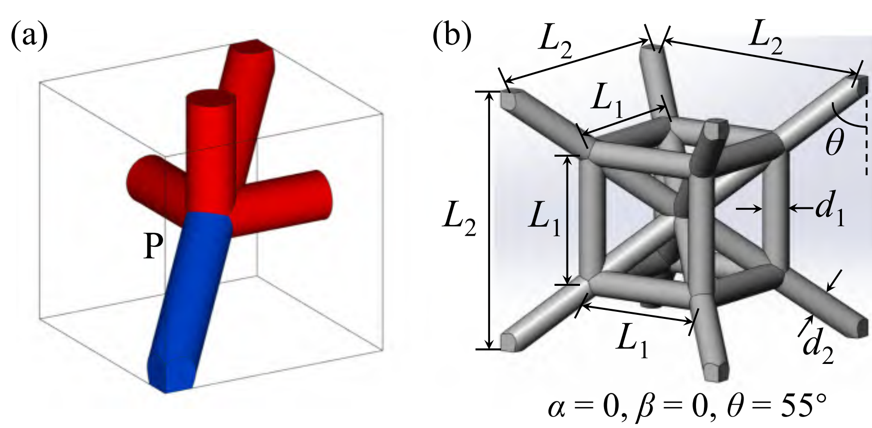

Fig. 3. Geometrical features of the CM lattices. (a) 1/8 subdivision of the unit cell with an SC-BCC core, and (b) geometrical parameters of the CM unit cell with $\alpha = \beta = 0$ and $\theta = 55^\circ$.

between the exterior cell struts and the z-axis. These geometric parameters remain consistent across all CM unit cells, regardless of core type.

The relative density $\overline{\rho}$ of the lattice cell is defined as

$$\overline{\rho} = V_s / V_{uc},$$

where V_s is the volume of solid material in the unit cell, V_{uc} is the nominal volume of the unit cell, taken as L_2^3 in this study.

2.2. Fabrication and mechanical testing

The lattice structures with various geometric configurations were fabricated using a LiM-X260 SLM machine with 316L stainless steel, chosen for its excellent ductility. The 316L powder size falls in a range from 15 μm to 53 μm. The SLM process utilizes a laser power of 195 W, scanning speed of 1080 mm/s, powder layer thickness of 20 μm, and hatch distance of 90 μm. To prevent oxidation during fabrication, the SLM chamber was filled with high-purity argon. A stainless steel substrate plate, preheated to 200 °C, was used to support the structures. A stripe scanning strategy with 67° layer rotation was applied. The fabricated lattice samples, comprising 5 × 5 × 5 unit cells with the unit cell geometry $d_1 = d_2 = 0.5$ mm and $L_2 = 2L_1 = 5$ mm, exhibit excellent manufacturability and precise structural features (Fig. 4).

Quasi-static compression tests were conducted using an MTS 370.10 universal testing system (100 kN force capacity) to examine mechanical behaviors of various lattice structures (Fig. 5). Samples were compressed along the build direction at a constant displacement rate of 0.025 mm/s. Reaction forces and platen displacements were recorded to calculate engineering stress (reaction force divided by the sample's initial lateral area, L_2^2) and engineering strain (displacement divided by the sample's initial height, L_2). The deformation process was documented at 1 fps using a digital camera. Each sample was tested twice to ensure reliability.

2.3. Energy absorption indicators

Three key indicators derived from the force-displacement curves are introduced to evaluate the energy absorption capabilities of the lattice structures [40]. Representing material toughness, the energy absorption (EA) is the area under the load-displacement curve, corresponding to the strain energy stored during compression, expressed as

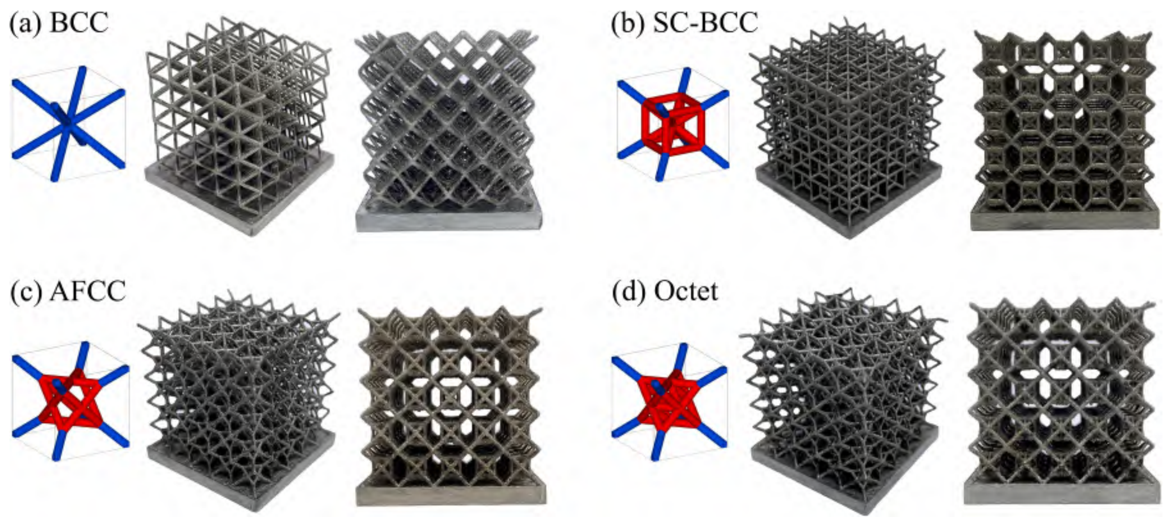

Fig. 4. Lattice designs and corresponding SLM-fabricated samples: (a) BCC, (b) SC–BCC, (c) AFCC, and (d) octet. Each panel shows the unit cell design (left), along with isometric (center) and front (right) views of the printed sample.

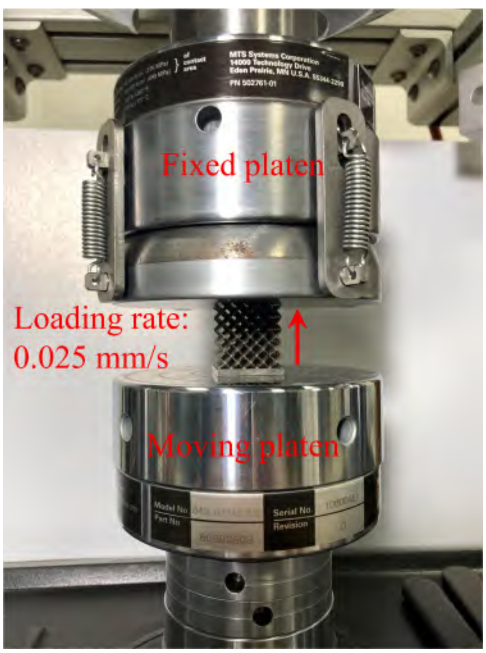

Fig. 5. Quasi-static compressive experiments with a constant displacement rate of 0.025 mm/s.

$$\mathrm{EA} = \int_0^U F(s)\mathrm{d}s,$$

where F is the compressive force, s the displacement, and U the effective deformation distance.

Specific energy absorption (SEA) normalizes EA by the structure mass m, measuring energy absorbed per unit mass as

$$\mathrm{SEA} = \mathrm{EA}/m.$$

SEA is a key metric for comparing energy absorption across different structures.

Mean crushing force P_m is defined as the average compressive force over the effective deformation range, and is given as

$$P_\mathrm{m} = \mathrm{EA}/U.$$

3. Experimental results

This section presents experimental results of both novel CM lattices and conventional BCC lattice under compression. We systematically analyze stress-strain responses, specific load-displacement relationships, energy absorption performance, and structural deformation evolution processes.

Fig. 6 presents the compressive engineering stress-strain curves for the fabricated lattice structures. The conventional BCC lattice demonstrates three distinct deformation stages: linear elasticity, a plastic plateau, and densification. In the elastic stage, stress increases linearly with strain until yielding, followed by a stable plastic plateau where plastic zones progressively form in the struts. The plastic plateau, characterized by limited strain hardening, results in hardening modulus degradation and slow strength growth. Densification occurs at higher strains, marked by a sharp stress rise as the structure fully compresses. The bending-dominated nature of the BCC lattice is evident in its long, stable plateau, maintaining stability up to 60 % compression ratio, consistent with prior studies [27,41].

In contrast, the CM lattices exhibit multi-step deformation with five distinct stages. After a short elastic deformation stage, an initial plastic plateau extends to 30 % compressive strain, followed by a secondary strengthening stage, characterized by a significant stress increase. Around 40 % strain, a second plastic collapse period with stress

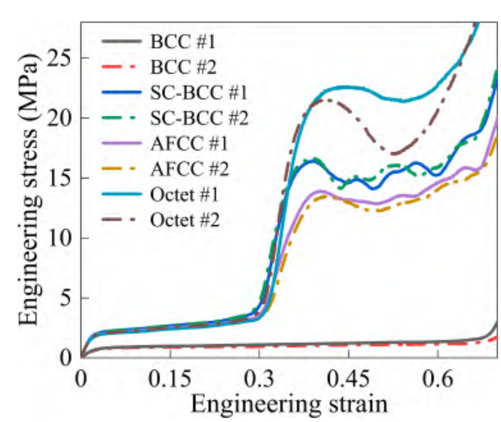

Fig. 6. Compressive engineering stress-strain curves for four types of lattice structures. Symbols #1 and #2 represent two repeated tests. The CM lattices exhibit distinct deformation stages compared to the conventional BCC lattice.

fluctuations occurs, leading to the densification stage. The second plastic collapse is less stable than the first due to increased strut failures after the secondary strengthening phase.

The onset of secondary strengthening occurs at similar strain levels across the CM lattices, suggesting it is independent of the core architecture, though the magnitude and stability of the secondary strengthening and subsequent collapse stages vary significantly with the core design. Among the CM lattices considered here, the octet-based configuration demonstrates the highest stress responses, indicating superior mechanical performance.

To account for mass differences among the structures, specific load versus compressive displacement curves are plotted in Fig. 7a. The specific load, defined as the reaction force normalized by structural mass, emphasizes the mechanical efficiency of the CM lattices. These lattices exhibit pronounced secondary strengthening and outperform the BCC lattice under large deformation. A magnified view of the initial 30 % strain range (Fig. 7b) shows that the CM lattices achieve higher specific loads than the BCC lattice during the plastic plateau. Among these CM designs, the fabricated octet structure has a significantly greater mass than the SC-BCC and AFCC variants. While the three CM lattices display similar stress responses within the initial 30 % compressive strain (Fig. 6), the octet's specific load appears lower in this stage due to its higher mass (Fig. 7b). Beyond 30 % strain, the octet lattice exhibits a substantially higher stress response compared to the other two CM lattices (Fig. 6), and its mass only partially offsets this advantage in specific load (Fig. 7a). Overall, the specific load trends in Fig. 7a remain consistent with the stress behaviors observed in Fig. 6.

Energy absorption analysis at 70 % compressive strain (Table 1) further underscores the advantages of the CM designs. SEA and EA in the CM lattices exceed those of BCC lattices by 4 to 5 times and 8 to 13 times, respectively. The octet-based CM lattice demonstrates the highest energy absorption. Additionally, mean crushing forces P_m for the CM lattices are improved by 7 to 12 times compared to the BCC lattice. These findings confirm that the CM design, incorporating varied core cell architectures, delivers substantial enhancements in energy absorption and load-bearing capacity.

Additionally, the absorbed energy per unit volume W_D up to the densification stage corresponds to the area under the engineering stress-strain curve in Fig. 1b as

$$W_D = \int_0^{\varepsilon_D} \sigma d\varepsilon,$$

where σ is the engineering stress, ε is the engineering strain, and ε_D is the densification engineering strain (Fig. 1b). Based on the multi-step compressive response, W_D can be decomposed as

$$W_D = W_I + W_{II},$$

Table 1
Energy absorption indicators of lattice structures with different core designs.

Specimen	SEA (J/g)	EA (J)	P_m (kN)
BCC#1	1.877	12.651	0.723
BCC#2	1.950	10.881	0.622
SC-BCC#1	10.276	108.309	6.189
SC-BCC#2	10.424	109.869	6.278
AFCC#1	9.828	93.563	5.346
AFCC#2	9.504	89.243	5.100
octet#1	12.186	142.576	8.147
octet#2	11.471	135.931	7.768

where W_I represents the energy absorbed during the elastic and plastic plateau stages, and W_{II} corresponds to the energy absorbed during the secondary hardening and plastic collapse stages. Since energy absorption is primarily governed by the plastic plateau and collapse stages, W_I and W_{II} can be approximated as

$$W_I \approx \sigma_p \varepsilon_h \quad \text{and} \quad W_{II} \approx \sigma_c(\varepsilon_D - \varepsilon_h),$$

where σ_p is the average plateau stress, ε_h is the engineering strain for secondary hardening onset, σ_c is the plastic collapse stress in Fig. 1b Therefore, the total absorbed energy per unit volume can be estimated as

$$W_D \approx \sigma_p \varepsilon_h + \sigma_c(\varepsilon_D - \varepsilon_h).$$

This estimation enables energy absorption quantification from the engineering stress-strain curves in Fig. 6. The unit volume energy absorption is calculated as 7.477 J/cm^3 for SC-BCC, 6.312 J/cm^3 for AFCC, and 9.796 J/cm^3 for the octet design. When scaled by the nominal structural volume (2.5^3 cm^3), the corresponding total energy absorption capacities are 116.828 J (SC-BCC), 98.625 J (AFCC), and 153.063 J (octet), closely aligning with the experimental values reported in Table 1. This simplified approach provides an efficient means for evaluating the energy absorption capabilities of the CM designs and supports the development of multifunctional, energy-dissipating lattice structures.

Fig. 8 presents the deformation and failure processes of the BCC and CM lattice structures at different values of the engineering strain ε. To provide a comprehensive comparison and deeper insight into failure mechanisms, experimental results are presented alongside finite element simulations, with details of the numerical analysis provided in Section 4.

For the conventional BCC lattice, the plastic plateau is marked with the formation and propagation of a local shear band (dashed lines) oriented at 45° to the loading axis, as shown in Fig. 8a. This shear band governs excessive plastic deformation and eventual strut collapse, leading to cell densification. From the simulation results in Fig. 8a, at a lower strain level of $\varepsilon = 0.15$, stress concentrations primarily occur near strut intersections, with minimal plastic deformation in the central

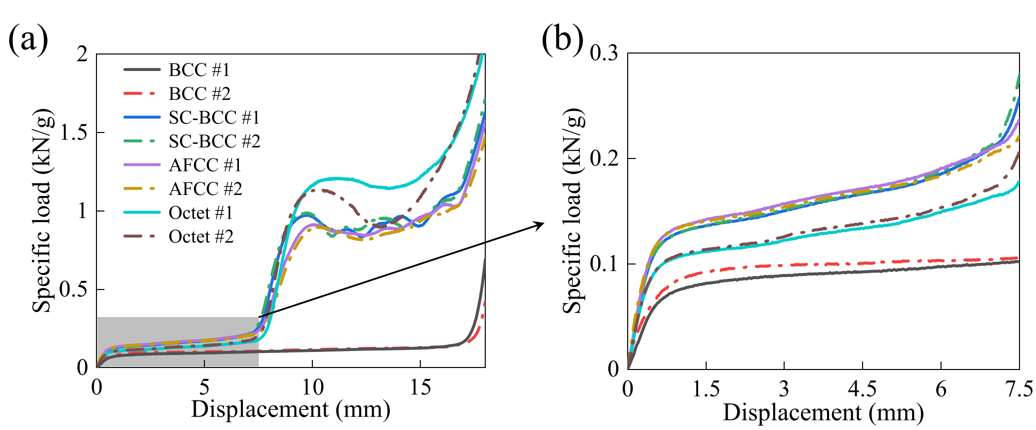

Fig. 7. Specific load–displacement curves for various lattice architectures. (a) Responses under 70 % compressive strain. (b) A magnified view of (a) under a 30 % compressive strain.

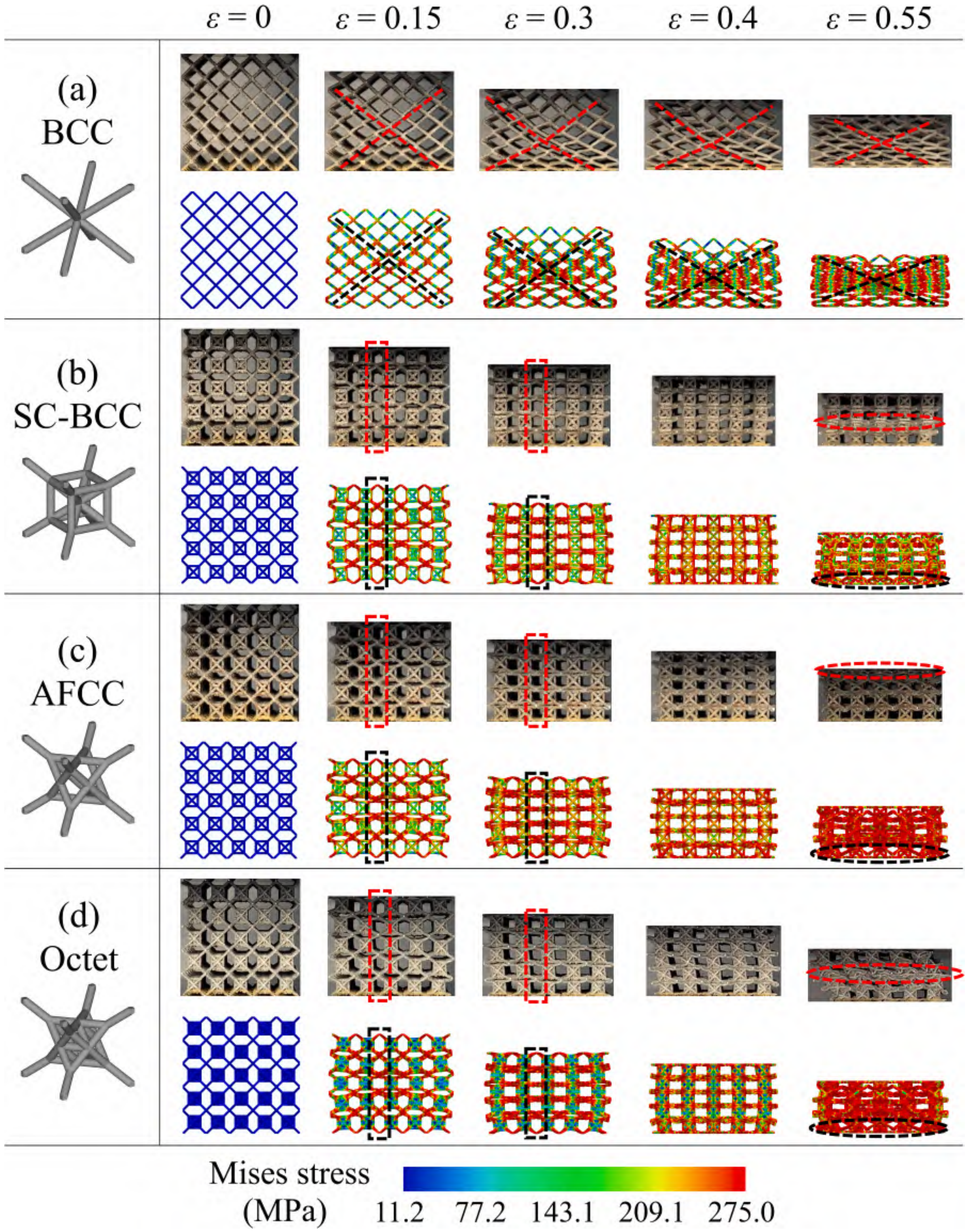

Fig. 8. Compressive deformation evolution of the lattice samples from experimental and simulation results. In (a), dashed lines indicate the formation of local shear bands. In (b)–(d), dashed rectangles highlight localized plastic deformation in the exterior cells, while dashed ellipses indicate the layer-by-layer failure behavior.

regions of individual struts. Both the experimental and simulation results in Fig. 8a show that cells near the shear band exhibit severe plastic distortions at $\varepsilon = 0.55$. The plastic plateau, characterized by limited strain hardening, results in hardening modulus degradation and slow strength growth, reflecting the bending-dominated nature of the BCC lattice.

In contrast, the CM lattices (Fig. 8b-d) display distinct deformation behaviors. The experimental and simulation results indicate that local plastic deformation initiates and evolves within the exterior BCC cells (dashed rectangles), leaving the embedded core cells largely intact, up to 30 % engineering strain. This deformation mode results in the first plastic plateau. At 40 % strain, the embedded core cells begin to dominate the deformation process through contact, forming vertical columns linked by exterior struts and giving rise to secondary hardening behavior. By $\varepsilon = 0.55$, layer-by-layer plastic collapse occurs predominantly in these vertical core columns (dashed ellipses) until final compaction. Additionally, visible lateral expansion occurs in the central regions, attributed to the plastic hinge rotation of the exterior struts.

Throughout compression, the CM lattices demonstrate more complex and distinct deformation stages than the BCC lattice, highlighting their enhanced structural performance.

The deformation process captured with experiments and simulations in Fig. 8 demonstrates that the secondary hardening and plastic collapse stages are primarily governed by the embedded core architecture. The observed stress differences among the three CM lattice structures during the plastic collapse stage (Fig. 6) can be directly attributed to the distinct mechanical behavior of their respective cores. Specifically, the octet core, which is stretching-dominated, inherently provides greater plastic collapse strength than the bending-dominated SC-BCC and AFCC cores [14].

The results demonstrate that the CM design effectively activates secondary hardening behavior and delays the propagation of localized deformation bands, a common limitation in conventional BCC lattices. This mitigates the extended stress plateau with low hardening modulus observed in BCC lattices under finite deformations. By leveraging the separation of exterior and core cells, multi-step deformation, including additional strengthening stages, is achieved, enhancing structural strength and energy absorption. Although the embedded core cells increase relative density, they substantially improve the overall mechanical performance.

4. Numerical simulations

This section develops finite element models to simulate the structural responses of the novel CM lattices and conventional BCC lattice under finite and small compressive strains. Section 4.1 details the simulation methodology using a multi-cell model for finite-strain behavior and a single unit-cell model for small-strain behavior, while Section 4.2 analyzes the simulated large deformation responses and elastoplastic small-strain responses.

4.1. Finite element models

Finite element analysis (FEA) was conducted to examine the deformation behavior and failure mechanisms of four lattice structures under uniaxial compression. The simulations utilized an elastoplastic material model for 316L stainless steel, with the following properties: density of 7.8 g/cm^3, Young's modulus $E_b = 150$ GPa, Poisson ratio of 0.3, initial yield stress $\sigma_b = 225$ MPa, and hardening modulus of 950 MPa [27].

4.1.1. Multi-cell model

Finite compressive engineering strain behaviors were analyzed using a $5 \times 5 \times 5$ multi-cell model in Abaqus/Explicit. To optimize computational efficiency, only one-quarter of the structure was simulated, with symmetric boundary conditions applied [41,42]. Compression was induced by two rigid plates: the lower plate was fixed, while the upper plate moved downward at a constant velocity of 1 m/s (Fig. 9a). Although this loading rate exceeds the experimental value, additional simulations (not shown) confirm that the ratio of kinetic to internal energy remained below 5 %, validating quasi-static conditions. Semi-automatic mass scaling was used to accelerate computations. Surface-to-surface contact was defined between the plates and the lattice, and a general explicit contact algorithm was applied to all lattice surfaces to prevent strut self-penetration. The friction coefficient was set to 0.2. The lattice was meshed using 4-node full-integration linear tetrahedral elements (C3D4) with an average element size of 0.15 mm. A mesh sensitivity analysis was conducted using element sizes of 0.15 mm and 0.2 mm, with distortion controls applied to ensure numerical accuracy. Hourglass effects—artificial zero-energy deformation modes present in reduced integration schemes—were eliminated by adopting full integration elements.

Strut failure was modeled using the damage initiation and evolution criteria. Damage initiation is governed by the ductile damage criterion, defined by the dimensionless parameter $\omega = \sum \left(\Delta\overline{\varepsilon}_p/\overline{\varepsilon}_p^D\right)$, where $\Delta\overline{\varepsilon}_p$ is the increment of equivalent plastic strain and $\overline{\varepsilon}_p^D$ is the equivalent plastic strain at the onset of damage, set to 0.3 in our simulations. Damage initiation occurs when $\omega = 1$, and the subsequent damage evolution is described by a damage variable D ($0 \le D \le 1$). The damage initiates at $D = 0$ and the complete failure is reached at $D = 1$. The damage variable D follows a linear evolution law with respect to the equivalent plastic displacement $\overline{u}_p$. The rate for $\overline{u}_p$ is determined by $\dot{\overline{u}}_p = L_e\dot{\overline{\varepsilon}}_p$, where L_e is the element length and $\dot{\overline{\varepsilon}}_p$ is the rate of the equivalent plastic strain. $\overline{u}_p$ vanishes before the damage initiates, and reaches the critical value $\overline{u}_p^f$ at the complete failure. The displacement value for $\overline{u}_p^f$ is taken as the element size in our simulations.

4.1.2. Single unit cell

To simulate the elastoplastic behavior of the lattice structures under small compressive strains, a single unit cell model was developed using the Abaqus/Standard implicit solver. The unit cell was discretized with C3D4 elements at an average element size of 0.1 mm, with over 5×10^4 elements per model to ensure numerical accuracy. Fig. 9b illustrates the

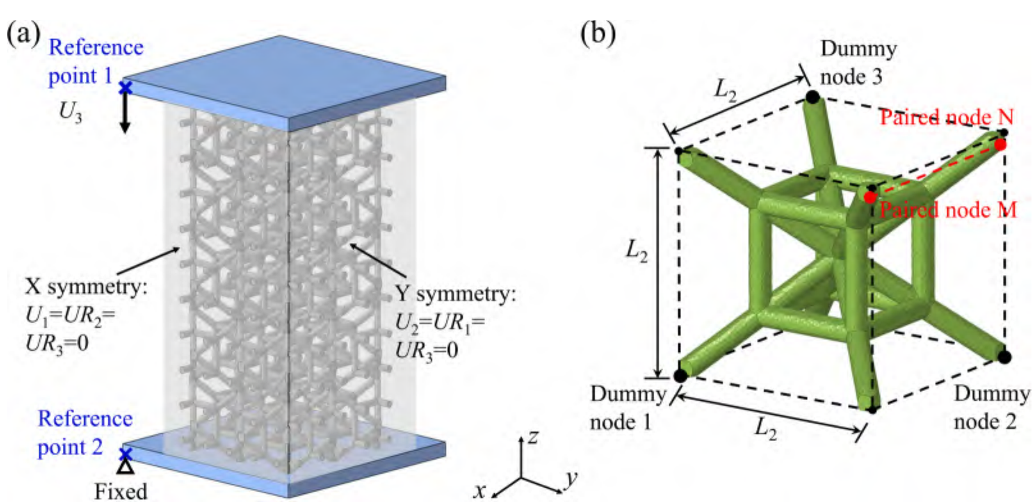

Fig. 9. Finite element simulation models. (a) Quarter multi-cell model with symmetric constraints, and (b) unit cell meshed model with periodic boundary conditions. U_1, U_2, and U_3 denote displacements along the x, y, and z directions, respectively. UR_1, UR_2, and UR_3 represent rotations about the x, y, and z directions, respectively.

meshed SC-BCC-based unit cell.

Periodic boundary conditions were applied to the unit cell in the *x, y*, and *z* directions, using three dummy nodes for displacement control. For paired nodes M and N on the surfaces orthogonal to the *x*-direction, their position vectors $\mathbf{x}_M$ and $\mathbf{x}_N$ satisfy $\mathbf{x}_M - \mathbf{x}_N = L_2\mathbf{n}_x$, where L_2 is the unit cell size, and $\mathbf{n}_x$ is the unit normal vector in the *x*-direction. Their displacements $\mathbf{u}_M$ and $\mathbf{u}_N$ are constrained by

$$\mathbf{u}_M - \mathbf{u}_N = L_2\mathbf{E}\cdot\mathbf{n}_x, \tag{1}$$

where $\mathbf{E}$ is the macroscopic strain tensor. In Abaqus, equation constraints are implemented for nodes M, N and a dummy node, leading to

$$\mathbf{u}_M - \mathbf{u}_N = \mathbf{u}_{DN1}, \tag{2}$$

where $\mathbf{u}_{DN1}$ is the displacement vector of the first dummy node. Similar constraints were imposed on other paired nodes and dummy nodes. These relations enable the macroscopic strain tensor components to be determined entirely by the degrees of freedom of the dummy nodes.

Two loading scenarios were employed to derive the homogenized elastic constants: uniaxial compression and pure shear, both with a macroscopic strain magnitude of 10^{-4}. Additionally, elastoplastic responses under a uniaxial compressive engineering strain of 4 % were simulated using unit cell models to analyze initial yield behavior.

For the cubic-symmetry lattice cell with its principal directions aligned with the coordinate axes in Fig. 9b, the homogenized elastic tensor is characterized by three independent components C_1, C_2, and C_3 as [43]

$$\begin{bmatrix}\sigma_{11}\\ \sigma_{22}\\ \sigma_{33}\\ \sigma_{23}\\ \sigma_{31}\\ \sigma_{12}\end{bmatrix} = \begin{bmatrix}C_1 & C_2 & C_2 & 0 & 0 & 0\\ C_2 & C_1 & C_2 & 0 & 0 & 0\\ C_2 & C_2 & C_1 & 0 & 0 & 0\\ 0 & 0 & 0 & C_3 & 0 & 0\\ 0 & 0 & 0 & 0 & C_3 & 0\\ 0 & 0 & 0 & 0 & 0 & C_3\end{bmatrix}\begin{bmatrix}\varepsilon_{11}\\ \varepsilon_{22}\\ \varepsilon_{33}\\ \gamma_{23}\\ \gamma_{31}\\ \gamma_{12}\end{bmatrix},$$

where σ_{11}, σ_{22}, σ_{33}, σ_{23}, σ_{31}, and σ_{12} denote the macroscopic stress components of the unit cell, and ε_{11}, ε_{22}, ε_{33}, γ_{23} ($= 2\varepsilon_{23}$), γ_{31} ($= 2\varepsilon_{31}$), and γ_{12} ($= 2\varepsilon_{12}$) denote the corresponding macroscopic strain components, respectively, with subscripts 1, 2, and 3 indicating the *x, y*, and *z* directions.

From these components, the structure Young's modulus E, Poisson ratio ν, and shear modulus G along the structural principal direction are derived as

$$E = \frac{(C_1+2C_2)(C_1-C_2)}{C_1+C_2},\quad \nu = \frac{C_2}{C_1+C_2},\ \text{and}\ G = C_3.$$

The Zener anisotropic index A is introduced to quantify the degree of anisotropy in cubic-symmetry lattices as [44]

$$A = \frac{2C_3}{C_1-C_2},$$

where $A = 1$ represents an elastically isotropic material, and deviations indicate varying degrees of anisotropy.

4.2. Simulation results

4.2.1. Large deformation responses

Fig. 10 compares the engineering stress-strain curves obtained from experiments and simulations for four lattice types under large deformations. For the conventional BCC lattice, the simulated engineering stress-strain response aligns well with experimental results. Similarly, the novel CM lattices exhibit consistent trends in stress-strain evolution across numerical and experimental data. However, the strain range of the second hardening stage in simulations appears slightly delayed compared to experiments. This discrepancy may stem from manufacturing defects in experimental samples and early strut contact due to surface roughness. Additionally, beyond the second hardening stage, the simulations slightly underestimate the mechanical responses, likely due to limitations in the damage criterion used in the numerical model and deviations between the experimental samples and the idealized geometries assumed in simulations.

The simulated deformation processes of the four lattice structures under uniaxial compression at increasing engineering strain are shown in Fig. 8, alongside experimental images for direct comparison.

4.2.2. Elastoplastic small-strain responses

Herein, the structure Young's modulus along a given directional vector $\mathbf{n}$ is denoted as E_n, which equals E when $\mathbf{n}$ aligns with the principal direction of the lattice. The corresponding normalized modulus is defined as $\overline{E} = E_n/(\overline{\rho}E_b)$, and its spatial anisotropy for the four lattices is

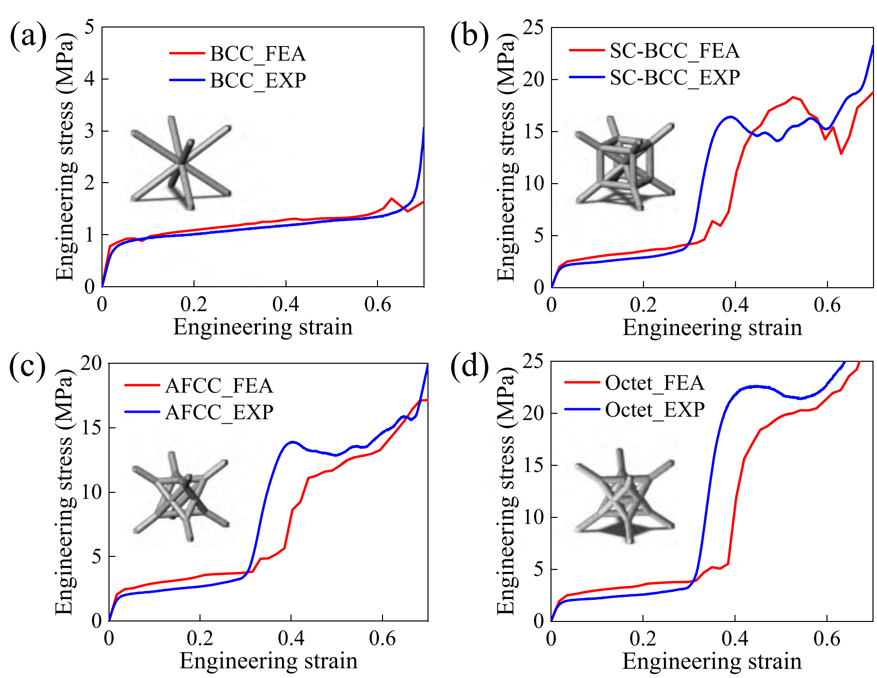

Fig. 10. Engineering stress-strain curves from experiments and FEA for different lattice structures: (a) conventional BCC, (b) SC-BCC, (c) AFCC, and (d) octet.

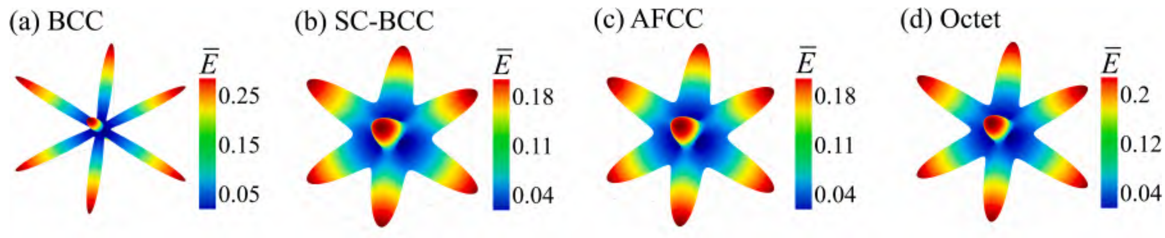

Fig. 11. Spatial distribution of the normalized Young's moduli for (a) BCC, (b) SC-BCC-based, (c) AFCC-based, and (d) octet-based CM lattices.

presented in Fig. 11, exhibiting distribution patterns similar to the conventional BCC lattice, with the stiffest response along the [111] diagonal direction and the softest along the [100] principal direction. The degree of elastic anisotropy is primarily governed by the strut arrangement.

The maximum and minimum normalized Young's moduli, along with Zener anisotropy index, are shown in Fig. 12a-c. Compared to the BCC lattice, the minimum normalized moduli of the SC-BCC, AFCC, and octet-based CM lattices are significantly improved. However, the maximum normalized moduli of the CM lattices are lower, attributed to the higher relative density of the novel CM designs. The Zener anisotropy indices for the CM lattices are notably reduced, indicating a mitigation of the elastic anisotropy seen in the BCC lattice.

Fig. 12d shows the directional dependence of the normalized Young's modulus in the (0 0 1) plane. The SC-BCC, AFCC, and octet-based CM lattices exhibit increased in-plane normalized moduli compared to the BCC lattice. The ratio of the maximum to minimum in-plane modulus ($\overline{E}_{[110]}/\overline{E}_{[100]}$) is 3.70 for the BCC lattice, 2.86 for SC-BCC, 2.91 for AFCC, and 3.09 for octet-based lattices. These results demonstrate that the novel CM designs enhance Young's modulus along the structural principal direction while reducing elastic anisotropy.

The normalized engineering stress, defined similarly to the normalized Young's modulus, and its evolution under uniaxial compressive strain of 0.04 for single unit cell simulations are shown in Fig. 13a. Compared to the BCC lattice, the CM lattices demonstrate enhanced initial plastic behavior. The normalized yield stress, defined at an engineering plastic strain of 0.2 %, is 0.0478 for the BCC lattice. In contrast, the normalized yield stress increases to 0.0721, 0.0734, and 0.0585 for SC-BCC, AFCC, and octet-based lattices, respectively, indicating improved initial yield strength in the CM designs. However, the octet-based lattice, with its higher relative density, exhibits a lower normalized yield stress than the SC-BCC and AFCC lattices. Additionally, the CM lattices enter the plastic yield stage earlier than the BCC lattice.

Fig. 13b shows the equivalent plastic strain distribution for all four lattices under a compressive strain of 0.04. In the BCC lattice, plastic dissipation occurs at the strut intersections, whereas the CM lattices exhibit plastic dissipation primarily at the exterior cell intersections. The CM lattices experience more significant plastic deformations at $\varepsilon = 0.04$, reflecting their earlier entry into the yield stage.

The above simulations demonstrate that incorporating various embedded core cells enhances the lattice structures in several key aspects, including improved elastic properties with reduced anisotropy, increased initial yield strength, and superior performance under large deformations. The multi-step deformation characteristics of the CM lattices enable the attainment of secondary hardening capacity.

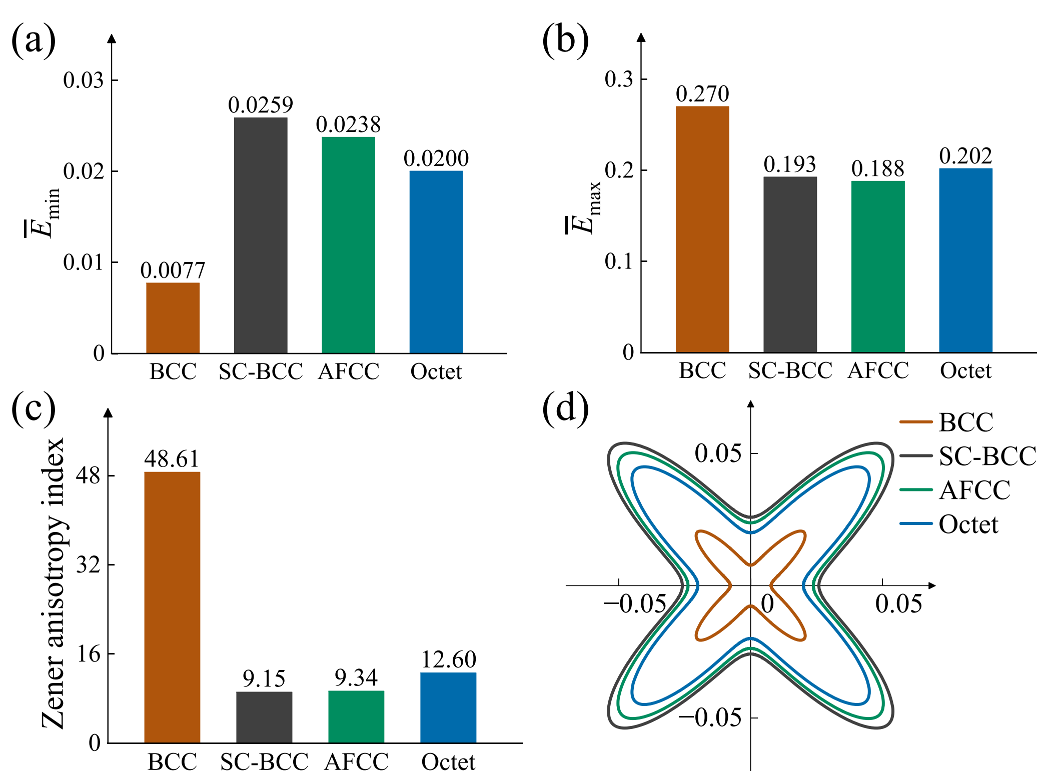

Fig. 12. Comparison of elastic anisotropy among the four lattice structures. (a,b) The minimum and maximum normalized Young's moduli, (c) Zener anisotropy index, and (d) normalized Young's modulus distributions in the (001) plane.

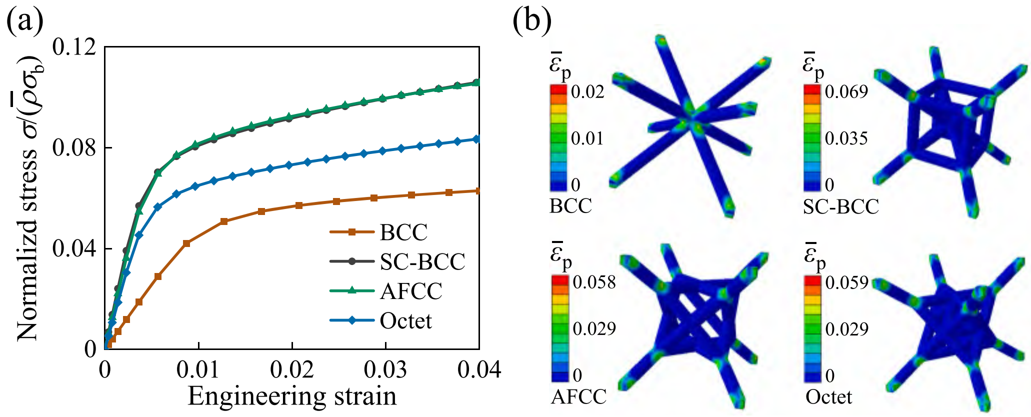

Fig. 13. Unit cell simulation results under 4 % uniaxial compressive engineering strain for the four lattices: (a) normalized engineering stress versus engineering strain curves, and (b) equivalent plastic strain distributions. Although the SC-BCC exhibits significantly higher equivalent plastic strain in (b), its engineering stress–strain response in (a) closely matches that of the AFCC due to normalization by the relative density $\bar{\rho}$.

5. Discussions

This section investigates the key geometric factors governing the mechanical response of octet-based CM lattices (Section 5.1) and elucidates the underlying mechanisms (Section 5.2).

5.1. Parametric analysis

The secondary hardening behavior of the CM lattices with embedded core cells, confirmed experimentally and numerically in Sections 3 and 4, is further analyzed through parametric studies to assess mechanical performance and energy absorption capabilities. Using the simulation model detailed in Section 4, the effects of key geometric parameters—diameter ratio α, size ratio β, and strut angle θ—are examined. For this analysis, the octet-based CM lattice is selected, with its geometric parameters systematically varied. An average mesh size of 0.2 mm is used to enhance computational efficiency, while maintaining the accuracy and other simulation settings from earlier sections.

5.1.1. Influence of diameter ratio α

Finite element models with varying core and exterior strut diameters are used to investigate the influence of the diameter ratio α on the mechanical performance of octet-based CM lattices. The parameters β and θ are fixed at 0 and 55°, respectively. A reference diameter of 0.5 mm is used for the struts, and α is varied by adjusting the core or exterior diameter. Specifically, $\alpha = 0$ corresponds to $d_1 = d_2 = 0.5$ mm, $\alpha < 0$ indicates $d_2 < d_1 = 0.5$ mm, and $\alpha > 0$ means $d_1 < d_2 = 0.5$ mm. For example, at $\alpha = -0.4$, the core and exterior strut diameters are 0.5 mm and 0.3 mm, respectively, while at $\alpha = 0.4$, they are 0.358 mm and 0.5 mm, respectively. The octet-based CM lattices with α values of -0.4, -0.2, 0, 0.2, and 0.4 are simulated under uniaxial compression to evaluate their mechanical responses.

Fig. 14a shows the engineering stress-strain curves for octet-based lattices with varying values of the diameter ratio α under compression. All lattices exhibit similar multi-step deformation behaviors, including an initial elastic stage, first plastic plateau, secondary hardening, plastic collapse, and ultimate densification. Despite differences in α, all lattices display secondary hardening after the compressive strain exceeds 35 %, marked by a rapid stress increase following the plastic plateau. The curve for $\alpha = 0$ serves as the reference, with changes in α significantly altering the response. When the exterior strut diameter decreases ($\alpha < 0$), the stress level at the first plastic plateau decreases, but the secondary hardening capacity remains unchanged. In contrast, reducing the core strut diameter ($\alpha > 0$) leads to a significant reduction in secondary hardening, while the first plateau stress level only decreases slightly. For $\alpha = 0.4$, the stress increment after the first plateau is

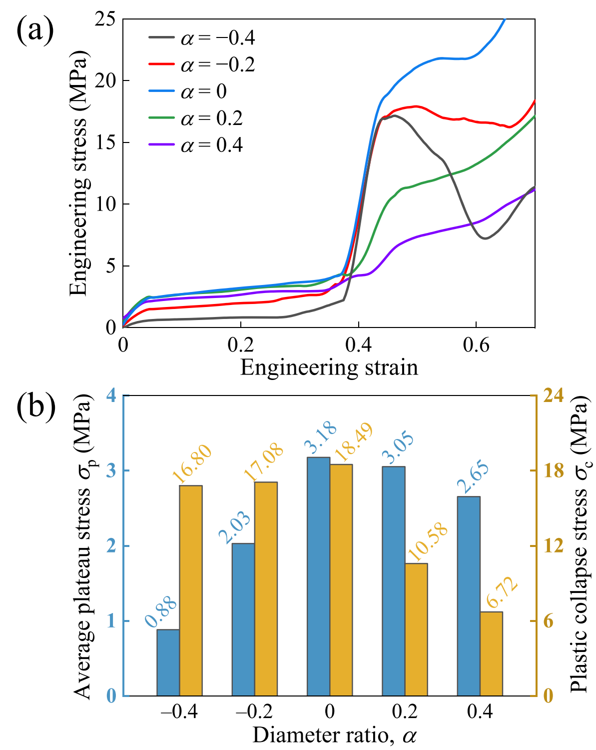

Fig. 14. Effects of the diameter ratio α on (a) the engineering stress-strain responses, and (b) the plastic plateau stress σ_p and plastic collapse stress σ_c of the octet-based lattices.

limited, and the secondary hardening effect is weaker compared to $\alpha = 0$. Furthermore, for both $\alpha > 0$ and $\alpha < 0$, plastic collapse occurs more readily after the secondary hardening stage due to the inability of the reduced strut diameters to sustain higher compressive loads.

The average plateau stress σ_p and the engineering stress σ_c at the onset of plastic collapse are used to quantitatively evaluate the impact of the diameter ratio α on the mechanical performance of octet-based lattices. Fig. 14b shows that negative values of α significantly reduce the average plateau stress. For instance, the plateau stress at $\alpha = -0.4$ decreases by 72.3 % compared to $\alpha = 0$, while at $\alpha = 0.4$, it only decreases by 16.7 %. The plastic collapse behavior is more sensitive to positive values of α; for $\alpha = 0.4$, the collapse stress is reduced by 63.7 % compared to $\alpha = 0$, whereas for $\alpha = -0.4$, it decreases by just 9.1 %. These results demonstrate that both the plastic plateau and secondary

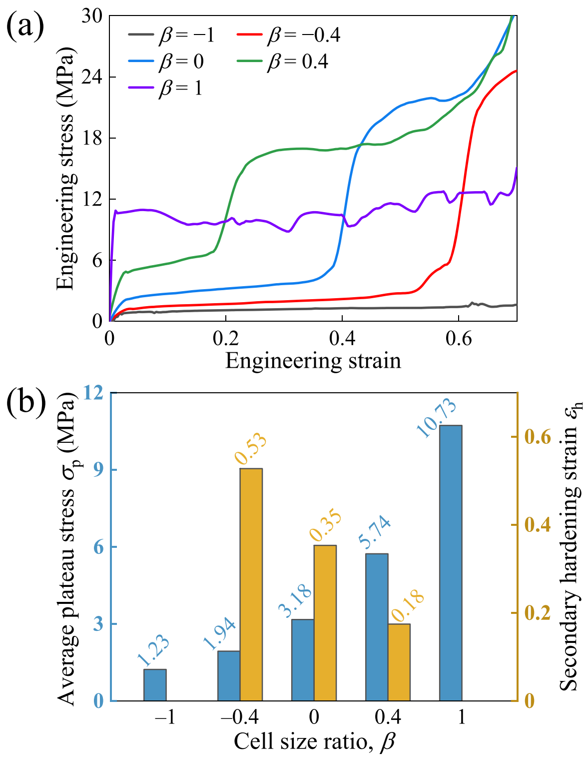

Fig. 15. Effects of the cell size ratio β on (a) the engineering stress-strain responses, and (b) the plastic plateau stress σ_p and secondary hardening onset strain ε_h of the octet-based lattices.

hardening capacity can be controlled by adjusting the diameters of the core and exterior struts.

5.1.2. Influence of cell size ratio β

This section explores the effect of the core cell size β on the mechanical responses of octet-based CM lattices. Fig. 15a indicates that β controls the proportion of the core cell within the unit cell, with increasing β resulting in a larger core volume. When $\beta = -1$, the structure resembles the conventional BCC lattice, while $\beta = 1$ corresponds to a complete octet lattice. The lattice models are constructed with fixed strut diameters ($d_1 = d_2 = 0.5$ mm) and angle ($\theta = 55°$), with β varied by adjusting the core cell size L_1 while keeping the unit cell size L_2 constant at 5 mm. Numerical simulations under uniaxial compression are conducted for different β values (−1, −0.4, 0, 0.4, and 1) to assess their impact on mechanical behavior.

Fig. 15a shows the engineering stress-strain curves for octet-based CM lattices at different β ratios. The variation in β significantly influences the structural deformation characteristics. For $\beta = -1$ (BCC lattice) and $\beta = 1$ (octet lattice), secondary hardening is absent, with the structure directly reaching the ultimate densification stage after a long plastic plateau. In contrast, for $\beta = -0.4$, 0, and 0.4, secondary hardening is clearly observed, characterized by a notable stress increase after the plastic plateau. The engineering stress-strain curve for $\beta = -1$ serves as the reference. As β increases, both initial Young's modulus and plastic plateau stress rise, approaching the values seen at $\beta = 1$. Additionally, the secondary hardening stage shifts leftward along the strain axis, and the plastic plateau strain range narrows with increasing β. Overall, the mechanical response of the CM lattice transitions toward that of the octet lattice as the proportion of core cells increases.

Fig. 15b presents the average plateau stress σ_p and engineering strain ε_h at the onset of secondary hardening, to assess the impact of the size ratio β. For the CM lattices, the plastic plateau stresses increase by 57.7 %, 158.5 %, and 366.7 % for β values of −0.4, 0, and 0.4, respectively, compared to the BCC lattice ($\beta = -1$). The secondary hardening strain ε_h decreases to 35 % and 18 % for $\beta = 0$ and 0.4, respectively, from −0.4. In contrast, secondary hardening strains are absent for the BCC and octet lattices due to the lack of a secondary hardening stage. Thus, both the plastic plateau stress and the strain at the onset of secondary hardening can be controlled by adjusting the size ratio β.

5.1.3. Influence of strut angle θ

The effect of the strut angle θ on the mechanical behavior of the octet-based CM lattices under [001] uniaxial compression is analyzed. In the simulations, the parameters $\alpha = 0$ ($d_1 = d_2 = 0.5$ mm) and $L_2 = 5$ mm are fixed. The exterior struts of the octet-based CM lattice for $\theta = 55°$ are rotated in the (110) diagonal plane with their length fixed, thus generating the lattice models for $\theta = 35°$, 45°, 65°, and 75° Variations in θ alter the core cell's shape and size. The core cell is cubic at $\theta = 55°$, increasing or decreasing θ causes the core cell to expand or shrink along the [001] direction.

Fig. 16a presents the engineering stress-strain curves of the octet-based CM lattices under compression at different values of θ. Across the range of 35° to 75°, all lattices demonstrate secondary hardening behavior, marked by a sharp stress increase following the plastic plateau. As θ increases, the secondary hardening stage shifts leftward. Additionally, increasing θ reduces the height of the exterior struts in the loading direction, shortening the strain range of the plastic plateau. This earlier onset of secondary hardening enhances load resistance and energy absorption, while the plastic plateau stresses remain relatively stable across θ variations.

As shown in Fig. 16b, the SEA value increases with θ, doubling at $\theta = 75°$ compared to $\theta = 35°$, highlighting the core cell's growing role in energy absorption with larger angles. Simultaneously, ε_h decreases sharply, dropping from 60 % to 11 % as θ rises from 35° to 75°, demonstrating that energy absorption is enhanced despite a reduced hardening strain. These findings indicate that tuning the strut angle enables control over the secondary hardening range and energy absorption performance of the CM lattices.

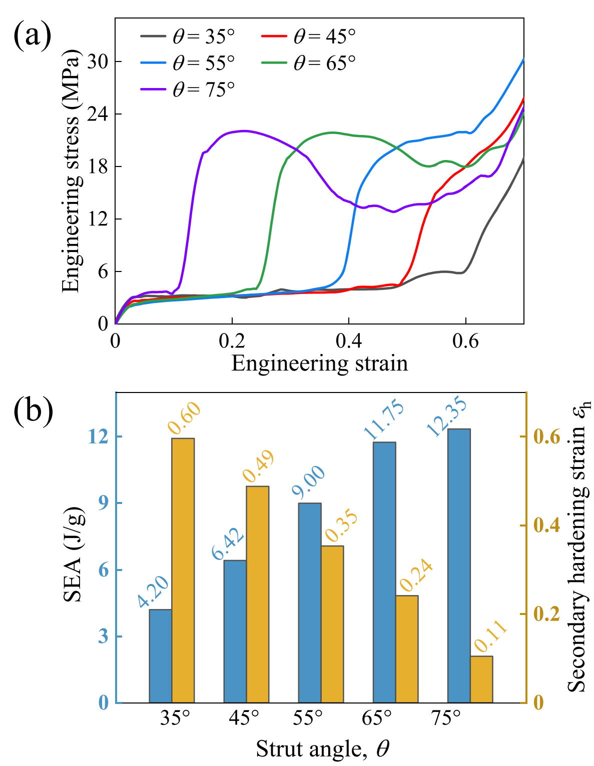

Fig. 16. Effects of the strut angle θ on (a) engineering stress-strain responses, and (b) SEA and secondary hardening onset strain ε_h of the octet-based lattices.

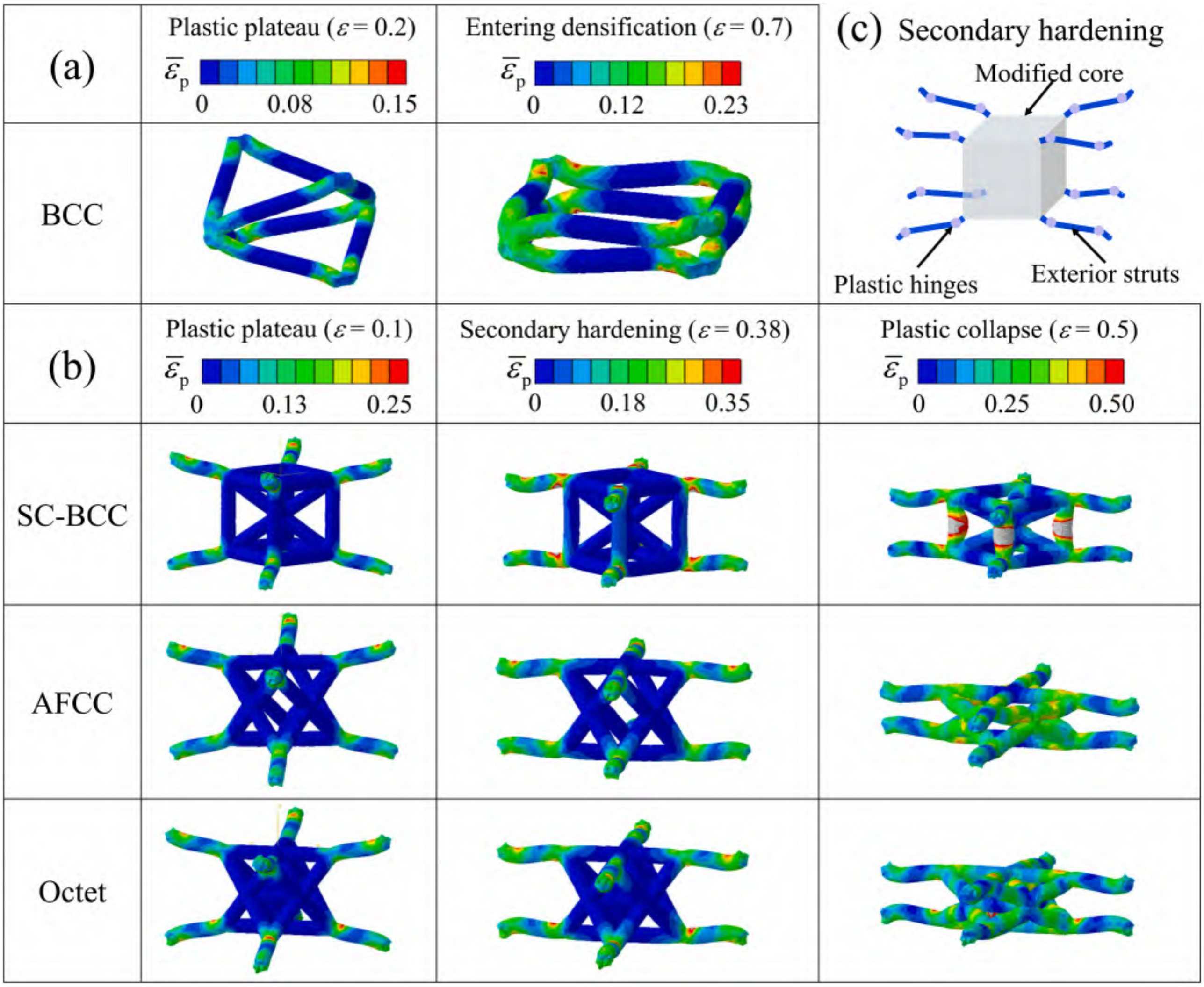

Fig. 17. Deformation modes of the central unit cell at various deformation stages: (a) BCC lattice and (b) SC-BCC, AFCC, and octet-based CM lattices. (c) Schematic illustration of the formation of the secondary hardening stage.

5.2. Deformation mechanisms

The mechanical response of lattice structures under finite deformation is intrinsically linked to the distribution and evolution of plastic deformation. Fig. 17 illustrates the equivalent plastic strain distributions and deformation modes in the central unit cell for four lattice types at various deformation stages. For the BCC lattice (Fig. 17a), plastic hinges form near the ends of individual struts during the plastic plateau, leading to a significant loss in load-bearing capacity. The final plastic collapse mechanism during densification aligns with prior predictions [17]. In contrast, the CM lattices (Fig. 17b) display partially similar characteristics during early deformation stages. Plastic hinges develop near the ends of exterior struts in the SC-BCC, AFCC, and octet-based CM lattices, resembling the BCC lattice behavior during the plastic plateau. However, the embedded core cells remain largely unaffected at this stage, allowing the exterior struts to undergo plastic collapse similar to the BCC lattice. This initial strut bending facilitates the emergence of secondary hardening behaviors driven by the core cells. As deformation progresses, the core cells dominate, undergoing plastic collapse and densification. The integration of embedded core cells enhances the mechanical performance of CM lattices, introducing counterintuitive hardening mechanisms that significantly improve their load-bearing and deformation capabilities.

A schematic diagram of the designed CM lattice in its undeformed state and at the onset of the secondary hardening stage is shown in Fig. 17c. Plastic hinges in the exterior struts are highlighted, while the central cubic region represents the embedded core cells. As discussed in Section 5.1, the secondary hardening response of the CM lattices can be controlled by adjusting the length and angle of the exterior struts, as these geometric changes dictate the spatial positioning of the plastic hinges. Given the significant property differences between the core cells and the exterior struts, plastic dissipation is primarily considered in the exterior struts before the secondary hardening stage. Then, the compressive displacement Δ_h and engineering strain ε_h at the onset of secondary hardening can be derived as

$$\Delta_h = \frac{L_2(1-\beta)}{2} - d_1, \quad \varepsilon_h = \frac{1-\beta}{2} - \frac{d_1}{L_2}, \quad \text{for changing } \beta, \tag{3}$$

Table 2
Comparison of predicted and simulated strains for varying β and θ.

β	Predicted	FEA	θ	Predicted	FEA
−0.4	0.6	0.53	35°	0.61	0.60
			45°	0.51	0.49
0	0.4	0.35	55°	0.40	0.35
			65°	0.27	0.24
0.4	0.2	0.18	75°	0.12	0.11

$$\Delta_h = \frac{\sqrt{3}}{2} L_2 \cos\theta - d_1, \quad \varepsilon_h = \frac{\sqrt{3}}{2}\cos\theta - \frac{d_1}{L_2}, \quad \text{for changing } \theta. \tag{4}$$

The predicted strains from Eqs. (3) and (4) align closely with simulation results presented in Figs. 15b and 16b (Table 2). Numerical simulations also reveal that the average plateau stress σ_p is tunable. For an increasing size ratio β, the plateau stress increases, while the hardening strain ε_h decreases. Conversely, decreasing the diameter of the exterior strut leads to a reduction in plateau stress with minimal change in the hardening strain. Additionally, the secondary hardening capacity improves with enhanced properties of the core cells. As shown in Fig. 6, the octet-based CM lattice exhibits superior secondary hardening performance due to the strengthening of its stretching-dominated octet core cell. Overall, the proposed CM lattice structure offers a tunable secondary hardening response, with both the plastic plateau and secondary hardening stage (Fig. 1b) adjustable through modifications to the exterior cells and embedded core cells.

The influence of geometric parameters β and θ on the strain range during the plastic plateau is further elaborated with simulation results in Fig. 18. The lattice structure consists of two mechanically distinct regions: a weaker exterior BCC framework and a stronger octet core. Prior to secondary hardening, plastic deformation primarily localizes in exterior struts, with unconstrained rotation of plastic hinges at their ends until octet-core contact occurs. The dashed boxes in Fig. 18 mark structures formed by the contacting octet-cores, and show that octet-based CM lattices exhibit consistent deformation modes at the critical engineering strain ε_h, which marks the onset of secondary hardening.

An increase in β shortens the exterior struts while keeping the strut angle θ fixed, effectively enlarging the octet core. This geometric change reduces both the critical compressive displacement Δ_h and secondary hardening onset strain ε_h (Eq. (3)), thereby narrowing the strain range of the plastic plateau—consistent with the trend shown in Fig. 18a. At

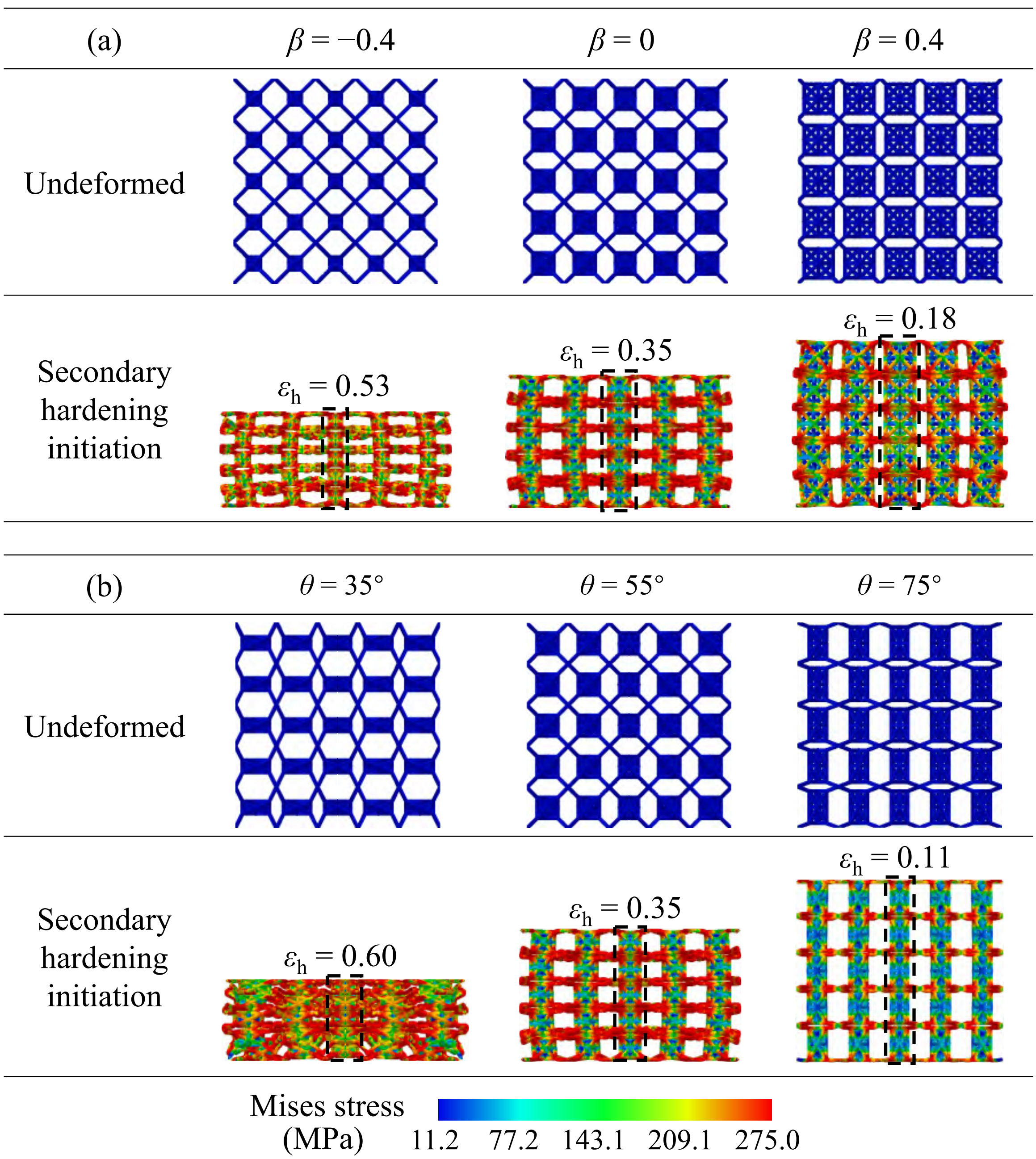

Fig. 18. Deformation modes at the engineering strain ε_h for secondary hardening onset in the octet-based CM lattices with varying (a) β and (b) θ.

lower values such as $\beta = -0.4$, the octet core becomes too small to manifest a distinct secondary hardening regime, resulting in a diminished plastic collapse region.

Similarly, increasing θ while holding the exterior strut length constant reduces both Δ_h and ε_h, as indicated by Eq. (4) and Fig. 18b. This also shortens the plastic plateau. At $\theta = 35^\circ$, the reduced height of the octet core along the loading axis obscures the boundary between secondary hardening and densification, similar to the behavior observed for $\beta = -0.4$. These results indicate that higher values of β and θ promote more distinct transitions between deformation stages, including secondary hardening, plastic collapse, and eventual densification.

6. Conclusions

This study proposes a novel core-modified (CM) lattice structure incorporating embedded core cells to achieve structural secondary hardening. The uniaxial compressive behaviors of the CM and conventional BCC lattices are explored through experimental tests and finite element simulations, complemented by a parametric analysis of the octet-based CM lattice.

Our results demonstrate that CM lattices (SC-BCC, AFCC, and octet-based) exhibit distinct secondary hardening at large strains—a feature absent in conventional BCC structures—effectively delaying localized deformation band propagation and significantly enhancing plastic deformation responses. Single-unit cell simulations further reveal that the CM lattices with embedded core cells demonstrate improved elastoplastic performance, including increased Young's modulus with reduced anisotropy and enhanced initial yield strength. Parametric analysis of the octet-based CM lattice highlights that its finite deformation response, including the plastic plateau and secondary hardening stage, can be tuned by modifying geometrical parameters such as diameter ratio, cell size ratio, and strut angle.

The multi-step deformation characteristics of CM lattices, enabled by core cell integration, allow spatial control of plastic hinges to tailor hardening responses under diverse loading conditions. By integrating secondary hardening mechanisms into traditional lattice designs, this approach enables the development of innovative lattice structures with enhanced load-bearing and multifunctional capabilities, paving the way for advanced engineering applications.

CRediT authorship contribution statement

Liming Huang: Writing – original draft, Investigation, Formal analysis. **Jiafei Pang:** Investigation. **Quanfeng Han:** Investigation. **Jianxiang Wang:** Investigation. **Xin Yi:** Writing – review & editing, Investigation, Funding acquisition, Formal analysis, Conceptualization.

Declaration of competing interest

The authors declare that they have no known competing financial interests or personal relationships that could have appeared to influence the work reported in this paper.

Acknowledgments

This work is supported by the National Natural Science Foundation of China (12588201 and 11988102). Computation resources supported by the High-performance Computing Platform of Peking University are acknowledged.

Data availability

Data will be made available on request.

References

[1] Ngo TD, Kashani A, Imbalzano G, Nguyen KTQ, Hui D. Additive manufacturing (3D printing): a review of materials, methods, applications and challenges. Compos B 2018;143:172–96. https://doi.org/10.1016/j.compositesb.2018.02.012.
[2] Wu W, Xia R, Qian G, Liu Z, Razavi N, Berto F, Gao H. Mechanostructures: Rational mechanical design, fabrication, performance evaluation, and industrial application of advanced structures. Prog Mater Sci 2023;131:101021. https://doi.org/10.1016/j.pmatsci.2022.101021.
[3] Hou W, He P, Yang Y, Sang L. Crashworthiness optimization of crash box with 3D-printed lattice structures. Int J Mech Sci 2023;247:108198. https://doi.org/10.1016/j.ijmecsci.2023.108198.
[4] Li S, Wang T, Chen S, Li Y, Zou Y, Cao B, Hu J, Tan X, Wang B. Compressive properties and biocompatibility of additively manufactured lattice structures by using bioactive materials. Thin-Walled Struct 2024;205:112469. https://doi.org/10.1016/j.tws.2024.112469.
[5] Huang L, Wan H, Han Q, Wang J, Yi X. Mitigating surface notches for enhanced fatigue performance of metallic gyroid structures via contour scanning. Int J Mech Sci 2025;286:109913. https://doi.org/10.1016/j.ijmecsci.2024.109913.
[6] Wei K, Chen H, Pei Y, Fang D. Planar lattices with tailorable coefficient of thermal expansion and high stiffness based on dual-material triangle unit. J Mech Phys Solids 2016;86:173–91. https://doi.org/10.1016/j.jmps.2015.10.004.
[7] Lakes R. Foam structures with a negative Poisson's ratio. Science 1987;235:1038–40. https://doi.org/10.1126/science.235.4792.1038.
[8] Guo M-F, Yang H, Ma L. Design and analysis of 2D double-U auxetic honeycombs. Thin-Walled Struct 2020;155:106915. https://doi.org/10.1016/j.tws.2020.106915.
[9] Frenzel T, Kadic M, Wegener M. Three-dimensional mechanical metamaterials with a twist. Science 2017;358:1072–4. https://doi.org/10.1126/science.aao4640.
[10] White BC, Garland A, Alberdi R, Boyce BL. Interpenetrating lattices with enhanced mechanical functionality. Addit Manuf 2021;38:101741. https://doi.org/10.1016/j.addma.2020.101741.
[11] Deshpande VS, Fleck NA, Ashby MF. Effective properties of the octet-truss lattice material. J Mech Phys Solids 2001;49:1747–69. https://doi.org/10.1016/S0022-5096(01)00010-2.
[12] Deshpande VS, Ashby MF, Fleck NA. Foam topology: bending versus stretching dominated architectures. Acta Mater 2001;49:1035–40. https://doi.org/10.1016/S1359-6454(00)00379-7.
[13] Leary M, Mazur M, Williams H, Yang E, Alghamdi A, Lozanovski B, Zhang X, Shidid D, Farahbod-Sternahl L, Witt G, Kelbassa I, Choong P, Qian M, Brandt M. Inconel 625 lattice structures manufactured by selective laser melting (SLM): mechanical properties, deformation and failure modes. Mater Des 2018;157:179–99. https://doi.org/10.1016/j.matdes.2018.06.010.
[14] Ashby MF. The properties of foams and lattices. Philos T R Soc A 2005;364:15–30. https://doi.org/10.1098/rsta.2005.1678.
[15] Fu M-H, Chen Y, Hu L-L. A novel auxetic honeycomb with enhanced in-plane stiffness and buckling strength. Compos Struct 2017;160:574–85. https://doi.org/10.1016/j.compstruct.2016.10.090.
[16] Berger JB, Wadley HNG, McMeeking RM. Mechanical metamaterials at the theoretical limit of isotropic elastic stiffness. Nature 2017;543:533–7. https://doi.org/10.1038/nature21075.
[17] Zhang H, Zhou H, Zhou Z, Zeng H, Zhang X, Yang J, Lei H, Han F. Energy absorption diagram characteristic of metallic self-supporting 3D lattices fabricated by additive manufacturing and design method of energy absorption structure. Int J Solids Struct 2021;226–227:111082. https://doi.org/10.1016/j.ijsolstr.2021.111082.
[18] Fu J, Ding J, Qu S, Zhang L, Wang MY, Fu MW, Song X. Improved light-weighting potential of SS316L triply periodic minimal surface shell lattices by micro laser powder bed fusion. Mater Des 2022;222:111018. https://doi.org/10.1016/j.matdes.2022.111018.
[19] Zhang L, Feih S, Daynes S, Chang S, Wang MY, Wei J, Lu WF. Energy absorption characteristics of metallic triply periodic minimal surface sheet structures under compressive loading. Addit Manuf 2018;23:505–15. https://doi.org/10.1016/j.addma.2018.08.007.
[20] Pham M-S, Liu C, Todd I, Lertthanasarn J. Damage-tolerant architected materials inspired by crystal microstructure. Nature 2019;565:305–11. https://doi.org/10.1038/s41586-018-0850-3.
[21] Yin S, Guo W, Wang H, Huang Y, Yang R, Hu Z, Chen D, Xu J, Ritchie RO. Strong and tough bioinspired additive-manufactured dual-phase mechanical metamaterial composites. J Mech Phys Solids 2021;149:104341. https://doi.org/10.1016/j.jmps.2021.104341.
[22] Guo W, Huang Y, Ritchie RO, Yin S. Dissipative dual-phase mechanical metamaterial composites via architectural design. Extreme Mech Lett 2021;48:101442. https://doi.org/10.1016/j.eml.2021.101442.
[23] Tian Y, Wang H, Chen Z, Wu Q, Yin S. Design principles for dual-phase lattice cylindrical tubes with excellent energy absorption capability. Compos Struct 2025;359:119015. https://doi.org/10.1016/j.compstruct.2025.119015.
[24] Cheng Q, Yin J, Wen J, Yu D, Tan VBC, Zhai W. Deformation control and energy absorption enhancement by hierarchical dual-phase design. Int J Mech Sci 2025;294:110257. https://doi.org/10.1016/j.ijmecsci.2025.110257.
[25] Lei H, Li C, Zhang X, Wang P, Zhou H, Zhao Z, Fang D. Deformation behavior of heterogeneous multi-morphology lattice core hybrid structures. Addit Manuf 2021;37:101674. https://doi.org/10.1016/j.addma.2020.101674.
[26] Chen Y, Li T, Jia Z, Scarpa F, Yao C-W, Wang L. 3D printed hierarchical honeycombs with shape integrity under large compressive deformations. Mater Des 2018;137:226–34. https://doi.org/10.1016/j.matdes.2017.10.028.

[27] Wang Z, Zhou Y, Wang X, Wei K. Compression behavior of strut-reinforced hierarchical lattice—Experiment and simulation. Int J Mech Sci 2021;210:106749. https://doi.org/10.1016/j.ijmecsci.2021.106749.
[28] Wang Y, Xu F, Gao H, Li X. Elastically isotropic truss-plate-hybrid hierarchical microlattices with enhanced modulus and strength. Small 2023;19:2206024. https://doi.org/10.1002/smll.202206024.
[29] Wu J, Yang F, Li L, Li P, Xu X, Zhang Y. Multi-feature bionic gradient hierarchical lattice metamaterials with multi-synergistic crushing mechanisms. Int J Mech Sci 2024;283:109383. https://doi.org/10.1016/j.ijmecsci.2024.109383.
[30] Wang H, Lu Z, Yang Z, Li X. In-plane dynamic crushing behaviors of a novel auxetic honeycomb with two plateau stress regions. Int J Mech Sci 2019;151:746–59. https://doi.org/10.1016/j.ijmecsci.2018.12.009.
[31] Li X, Li Z, Guo Z, Guo Z, Mo Z, Li J. A novel hybrid star honeycomb with individually adjustable second plateau stresses. Compos Struct 2025;356:118881. https://doi.org/10.1016/j.compstruct.2025.118881.
[32] Xu Z, Lu J, Gu X, Hou J, Liu J, Wu J. Mechanical performance and prediction of a novel reinforced octagonal honeycomb. Int J Mech Sci 2024;284:109758. https://doi.org/10.1016/j.ijmecsci.2024.109758.
[33] Kothari T, Liu X, Kobir MH, Yang Y, Tao F. Design and analysis of reinforced I-beam body-centered cubic lattices for enhanced energy absorption. Compos Struct 2025;355:118841. https://doi.org/10.1016/j.compstruct.2025.118841.
[34] Liu X, Suzuki A, Takata N, Kobashi M, Kato M. Dual plateau stress of C15-type topologically close-packed lattice structures additive-manufactured by laser powder bed fusion. Scr Mater 2021;202:114003. https://doi.org/10.1016/j.scriptamat.2021.114003.
[35] Ma X, Zhang N, Zhang C, Tian X. Mechanical behavior of a novel lattice structure with two-step deformation. Thin-Walled Struct 2024;197:111580. https://doi.org/10.1016/j.tws.2024.111580.
[36] Wang M, Wang Y, Wu J, Wang W. Experiment and numerical investigation on bio-inspired tube-plate hybrid lattice structure with dual-stress plateaus and enhanced energy absorption. Virtual Phys Prototyp 2025;20:e2500116. https://doi.org/10.1080/17452759.2025.2500116.
[37] Chen L, Chen T, Feng S, Cui CY, Cui XG, Lu JZ. Self-similar nesting strategy enables lattices achieve dual energy-absorbing plateaus. Int J Mech Sci 2024;276:109445. https://doi.org/10.1016/j.ijmecsci.2024.109445.
[38] Tancogne-Dejean T, Mohr D. Elastically-isotropic truss lattice materials of reduced plastic anisotropy. Int J Solids Struct 2018;138:24–39. https://doi.org/10.1016/j.ijsolstr.2017.12.025.
[39] Bai L, Zhang J, Chen X, Yi C, Chen R, Zhang Z. Configuration optimization design of Ti6Al4V lattice structure formed by SLM. Materials 2018;11:1856. https://doi.org/10.3390/ma11101856.
[40] Ha NS, Lu G. A review of recent research on bio-inspired structures and materials for energy absorption applications. Compos B 2020;181:107496. https://doi.org/10.1016/j.compositesb.2019.107496.
[41] Bai L, Gong C, Chen X, Sun Y, Xin L, Pu H, Peng Y, Luo J. Mechanical properties and energy absorption capabilities of functionally graded lattice structures: experiments and simulations. Int J Mech Sci 2020;182:105735. https://doi.org/10.1016/j.ijmecsci.2020.105735.
[42] Cao X, Duan S, Liang J, Wen W, Fang D. Mechanical properties of an improved 3D-printed rhombic dodecahedron stainless steel lattice structure of variable cross section. Int J Mech Sci 2018;145:53–63. https://doi.org/10.1016/j.ijmecsci.2018.07.006.
[43] Bonatti C, Mohr D. Smooth-shell metamaterials of cubic symmetry: anisotropic elasticity, yield strength and specific energy absorption. Acta Mater 2019;164:301–21. https://doi.org/10.1016/j.actamat.2018.10.034.
[44] Ranganathan SI, Ostoja-Starzewski M. Universal elastic anisotropy index. Phys Rev Lett 2008;101:055504. https://doi.org/10.1103/PhysRevLett.101.055504.